Liquid metal intercalation of epitaxial graphene: Large-area gallenene layer fabrication through gallium self-propagation at ambient conditions

S. Wundrack [1,*] D. Momeni [1] W. Dempwolf [3,4] N. Schmidt [2] K. Pierz [1] L. Michaliszyn [1] H. Spende [2,3] A. Schmidt [2,3] H. W. Schumacher [1] R. Stosch [1] and A. Bakin [2,3,†]

[1] *Physikalisch-Technische Bundesanstalt, Bundesallee 100, 38116 Braunschweig, Germany*

[2] *Institut für Halbleitertechnik, Technische Universität Braunschweig, Hans-Sommer Straße 66, D-38106 Braunschweig, Germany*

[3] *Laboratory of Emerging Nanometrology (LENA) der Technischen Universität Braunschweig, Langer Kamp 6 a/b, 38106 Braunschweig, Germany*

[4] *Institut für Technische Chemie, Technische Universität Braunschweig, Hagenring 30, 38106 Braunschweig, Germany*

(Received 28 June 2020; revised 2 December 2020; accepted 4 January 2021; published 19 February 2021)

We demonstrate the fabrication of an ultrathin gallium film, also known as gallenene, beneath epitaxial graphene on 6H-SiC under ambient conditions triggered by liquid gallium intercalation. Gallenene has been fabricated using liquid metal intercalation, achieving lateral intercalation and diffusion of Ga atoms at room temperature on square centimeter areas limited only by the graphene samples' size. The stepwise self-propagation of the gallenene film below the epitaxial graphene surface on the macroscopic scale was observed by optical microscopy shortly after the initial processing without further physical or chemical treatment. Directional Ga diffusion of gallenene occurs on SiC terraces since the terrace steps form an energetic barrier (Ehrlich-Schwoebel barrier), retarding the gallenene propagation. The subsequent conversion of the epitaxial graphene into quasi-free-standing bilayer graphene and the graphene-gallenene heterostack interactions have been analyzed by x-ray photoelectron spectroscopy and Raman measurements. The results reveal an alternative approach for the controlled fabrication of wafer-scale gallenene as well as for two-dimensional heterostructures and stacks based on the interaction between liquid metal and epitaxial graphene.

DOI: 10.1103/PhysRevMaterials.5.024006

I. INTRODUCTION

The fabrication of large-area high-quality graphene samples has opened new fields of research to investigate the feasibility of creating new two-dimensional crystal structures. This applies in particular to semiconductor materials as well as to the fabrication of van der Waals heterostructures exploring their physical interactions at the nanoscale of condensed matter [1–9].

Ever since the demonstration of graphene was first achieved in 2004 [10], a whole family of two-dimensional materials has been discovered and fabricated using the straightforward exfoliation technique [11–16]. For instance, hexagonal boron nitride (hBN) or transition-metal dichalcogenides (TMDCs) such as tungsten disulfide (WS_2) and molybdenum disulfide (MoS_2) can be easily obtained by exfoliation from their bulk single crystals based on breaking the weak interlayer bonding similar to that of graphite [14–16].

Among two-dimensional (2D) materials, elemental atomic layers of group III to group VI elements are gaining rapidly growing attention. Those classes of materials, so-called Xenes (silicene, phosphorene, stanene, etc.), cover a broad spectrum of physical properties from metallic to semiconducting, and they provide a wide range of potential applications in the areas of photonics, electronics, and energy conversion. Just recently, the fabrication of metallic gallenene has been demonstrated [17]. At present, however, fabrication approaches, as well as properties investigations of gallenene, are at an early stage of research.

Gallium (Ga) is a metallic element with an unusually low melting point of 29.7 °C [18,19] as compared to other metals. Strong electronic bonding states exist between two Ga atoms forming a Ga pair, whereas the bonding energy between Ga pairs is significantly lower [20]. Besides the liquid phase of Ga, several different solid-state modifications of Ga exist and are referred to as α- to γ-Ga phase occurring at defined pressure-temperature conditions [21] as well as in metastable supercooling phases [22,23]. The investigation of atomically thin Ga films on semiconducting substrates and their surface reconstruction behavior on these surfaces is still a matter of scientific studies [24]. The discovery of ultrathin gallium oxide sheets, as well as monochalcogenide gallium sulfide (GaS), has recently attracted attention since it provides an alternative approach of the exfoliation technique utilizing the liquid phase instead of a solid phase of a metal [25]. Carey *et al.* have exfoliated atomically thin layers of gallium oxide from the surface of the liquid phase of Ga onto an oxidized silicon wafer, which was previously hydrophobized with a silane to create a patterned gallium oxide layer. Using surface chemistry, they converted the oxide layer into two-dimensional GaS [25].

*stefan.wundrack@ptb.de
†a.bakin@tu-braunschweig.de

 ©2021 American Physical Society

Recently, Kochat *et al.* have demonstrated the exfoliation of "gallenene"—an atomically thin sheet of Ga—from the liquid Ga phase onto different substrates using the solid-melt exfoliation technique [17]. In this context, they demonstrated the extraction of the (010) and (100) crystal planes (zigzag and honeycomb-like structure) from α-Ga, which were stabilized at ambient conditions due to strong interactions with the underlying substrates as underpinned by density functional theory (DFT) calculations. The honeycomb phase of gallenene occurs even in an epitaxially grown monocrystalline bilayer, which is stabilized on the (0001) plane of gallium nitride (GaN) [26]. The gallenene layer has a thickness of only 0.55 nm and exhibits superconductivity at a higher transition temperature as compared to bulk Ga due to polarization effects from the underlying GaN substrate. Furthermore, the epitaxial growth of gallenene on a Si(111) surface has been demonstrated by Tao *et al.* [24]. Also, the conversion of Ga into 2D GaN semiconductor layers by the chemical process of ammonolysis is of technological interest, as described by Al Balushi *et al.*, and it was shown in [27]. There, a thin Ga layer was prepared by incorporation of Ga atoms between an epitaxial graphene sheet and the SiC substrate at high temperature employing the decomposition of trimethylgallium as the Ga source. Very recently, Briggs *et al.* have presented the intercalation of Ga, indium (In), and tin (Sn) atoms under epitaxial graphene [28]. The intercalation was carried out under vacuum conditions (300 Torr) using the evaporation of metals at high temperatures (700–800 °C). The diffusion of Ga atoms in the proposed confinement heteroepitaxy (CHet) approach was activated by high defect densities in pre-treated epitaxial graphene, which act as entrance slots for Ga atoms. Furthermore, the remaining Si dangling bonds on the SiC substrate promoted the detachment of the graphene buffer layer and conversion of epitaxial graphene into quasi-free-standing bilayer graphene (QFBLG).

The preliminary work of different research groups has shown a broad versatility of liquid Ga by downsizing the bulk material to the two-dimensional level. Based on our liquid metal intercalation technique (LiMIT) initially reported elsewhere [29], we demonstrate here an extremely simplified and a far more extensive large-scale deposition of gallenene at ambient conditions. The proposed technique deploys low defect density in epitaxial graphene and low-temperature synthesis, which allows large-area fabrication of gallenene films and *in situ* characterization of the gallenene propagation. The Ga intercalation takes place through micropipes of the 6H-SiC substrate. The self-propagation and diffusion process of Ga atoms occurs along the terraces of the 6H-SiC substrate and affects the entire sample.

Several analytical methods were used to investigate the physical properties of gallenene: optical microscopy, microreflection spectroscopy, scanning electron microscopy (SEM), x-ray photoelectron spectroscopy (XPS), and atomic force microscopy (AFM), as well as laser ablation inductively coupled plasma mass spectrometry (LA-ICP-MS). In addition, we used confocal micro-Raman spectroscopy to evaluate the interlayer interactions between gallenene and graphene, as well as van-der-Pauw measurements to assess their electrical properties.

II. MATERIALS AND METHODS

In this section, we discuss substrate fabrication and treatment. Epitaxial graphene was grown on the Si-face of SiC samples $(5 \times 10)\,\mathrm{mm}^2$ cut from a semi-insulating 6H-SiC wafer with a nominal miscut angle of about 0.06° toward the $(1\bar{1}00)$ surface. The graphene samples were prepared according to the polymer-assisted sublimation growth (PASG) technique, which involves polymer adsorbates formed on the SiC surface by liquid phase deposition from a solution of a photoresist (AZ5214E) in isopropanol followed by sonication and short rinsing with isopropanol. The graphene layer growth was processed at 1750 °C (argon atmosphere ∼1 bar, 6 min, zero argon flow) with pre-vacuum-annealing at 900 °C [30,31]. The applied PASG method allows the growth of large-area ultrasmooth, homogeneous monolayer graphene, with almost an isotropic resistance characteristic [32], thus it is very well suited as the basis for the fabrication of large-area two-dimensional gallenene sheets by solid-melt intercalation technique as described in this work. Commercial Ga (99.99 % purity) was purchased from Heraeus. See Sec. III.

Raman measurements of graphene and gallenene were acquired at ambient conditions with a Witec Alpha 300 RA (Witec GmbH) Raman spectrometer equipped with a frequency-doubled Nd:YAG laser emitting at 488 nm ($E_L = 2.54\,\mathrm{eV}$) and a 100× (N.A. 0.9) objective to focus the excitation laser onto the sample surface. A LabRAM Aramis Raman spectrometer (Horiba) has been used in the case of excitation wavelengths of 532 nm ($E_L = 2.32\,\mathrm{eV}$) and 633 nm ($E_L = 1.96\,\mathrm{eV}$). Confocal micro-Raman mappings were recorded over $(20 \times 20)\,\mu\mathrm{m}^2$ scan areas in backscattering mode using a piezodriven xy-stage (PI) and a scanning step size of 0.1 μm.

AFM measurement was carried out using the Nanostation AFM (S.I.S.), providing pronounced resolution for precisely resolving structures down to 0.25 nm and the AFM station of the Witec Alpha 300 RA (Witec GmbH).

SEM investigations were carried out inside a Tescan Mira 3 GMH FE-SEM. A high surface sensitivity was reached using acceleration voltages between 1 and 5 kV and small beam currents. The in-lens SE detector offered sufficient SNR, high contrast, and high resolution for the small working distances used. Besides the topographic information mainly provided by the asymmetrically mounted SE detector, the additional in-lens SE detector also images the work function (e.g., material variations) of the sample.

LA-ICP-MS mappings were measured by using a laser ablation system (NWR 213, New Wave Research Inc.), which is equipped with a frequency quintupled Nd:YAG deep UV laser emitting at 213 nm ($E_L = 5.82\,\mathrm{eV}$) focusing the laser with a pulse energy of about 0.1 mJ and a spot diameter of 20 μm. Ablated materials were investigated by means of a double-focusing magnetic sector field high-resolution ICP mass spectrometer (Element XR, Thermo Scientific Inc.), analyzing the isotopic ratios of ^{69}Ga and ^{71}Ga.

XPS measurements were obtained on an AXIS Supra system (Kratos Analytical Ltd.) using a monochromatized Al $K\alpha$ x-ray source. Survey scans were acquired using a pass energy of $E = 160\,\mathrm{eV}$ (not shown). High-resolution core-level spectra (C 1s, Si 2 p, and Ga 3 d) were obtained using a pass energy of $E = 20\,\mathrm{eV}$. Data analysis was performed using CasaXPS software.

III. RESULTS AND DISCUSSION

The presented experimental results of the gallenene characterization are divided into five subsections. In the first subsection, the fabrication process and the temporal intercalation steps of gallenene are described in general using optical microscopy. The topological and chemical characterization of the gallenene films is explained in the second subsection using AFM, SEM, XPS, LA-ICP-MS, and Raman spectroscopy. Further structural clarifications and investigations of the interactions between gallenene and graphene regarding strain and charge carrier doping follow in the third, fourth, and fifth subsections.

A. Intercalation process of gallenene beneath epitaxial graphene

A schematic representation of the fabrication process is depicted in Fig. 1(a), including the observed self-propagation of gallenene. Optical images of large gallenene-covered areas as well as from regions acquired shortly after the liquid metal intercalation are shown in Figs. 1(b) and 1(c). In general, the deposition of a sizeable gallenene layer has been achieved by depositing a droplet of liquid Ga ($V \approx 10\,\mu$L) onto the surface center of the SiC substrate [Fig. 1(a), I], which is covered with epitaxial graphene on top of the (0001) lattice plane of 6H-SiC. The latter consists of monolayer graphene and the buffer layer, which is covalently bonded to the Si-terminated side of the SiC substrate [30–32].

The liquid metal intercalation was initiated by placing the epitaxial graphene sample with a Ga droplet on its surface onto an object slide and heating them to 120 °C. This treatment results in a temperature gradient from the annealing source to the sample surface so that a lower surface temperature of the epitaxial graphene sample can be assumed. However, since a higher process temperature could cause structural lattice defects in the graphene, the mentioned process temperature has not been exceeded. The Ga droplet was spread only to the lower side of the sample by wiping the liquid metal across the substrate surface using a squeegee, as indicated in Fig. 1(a) (I).

Figure 1(b) (I–III) represents three stages of a typical time-dependent self-propagation of gallenene, recorded shortly after spreading the liquid Ga droplet and proceeding at room temperature. The color contrast in Fig. 1(b) (I–III) reveals large bright and dark areas across the substrate. Examining these regions by LA-ICP-MS measurements proves the existence of Ga unambiguously within the bright regions from its isotopic fingerprint (as shown later), while the dark areas correspond to nonintercalated epitaxial graphene grown on 6H-SiC. A stepwise broadening of the brightly colored areas can easily be observed using the red auxiliary line as the starting point. The propagation velocity of gallenene across the sample surface varies over time. Figure 1(b) (I–II) reveals a low propagation within the first 20 min including processing on the hot plate and cooling down to room temperature, followed by a significant increase in the subsequent period [Fig. 1(b), II–III], which resulted in complete coverage of the investigated area within the next 10 min [Fig. 1(b), III]. The corresponding time-lapse video of the gallenene self-propagation at room temperature, as shown in Fig. 1(b), is available in the supplemental material [33]. Figure 1(b) contains three images extracted from the video showing different states of the self-propagation of gallenene that occurred fitfully in a noncontinuous motion. The video, as well as Fig. 1(b) (III), reveals the existence of two different propagation directions of Ga atoms indicated by the vector $\vec{a}$, which is approximately aligned to the $(1\bar{1}00)$ lattice plane of the SiC substrate, and the vector $\vec{b}$, which is aligned parallel to the terrace steps of SiC as revealed by AFM measurements [Fig. 1(b), II inset]. The propagation velocity along $\vec{b}$ is significantly larger as compared to the direction of the vector $\vec{a}$. A detailed AFM analysis of the nonintercalated graphene surface shows an orthogonal direction of terrace steps to $\vec{a}$ having an average step height of 0.75 nm (Fig. S1 in the supplemental material) [33]. We therefore conclude that the diffusion of Ga atoms of gallenene is energetically favored along the SiC terrace ($\vec{b}$), whereas the terrace steps form an energetic barrier (Ehrlich-Schwoebel barrier) retarding the gallenene propagation along $\vec{a}$.

Figure 1(c) demonstrates that gallenene covers almost the entire width of the sample substrate while residues of Ga remain at the lower sample side. Finally, the self-propagation of gallenene affects the whole sample surface keeping the upper side of the sample free from any bulk Ga residues on the graphene surface. The upper region of the sample thus allows further analytical investigations (e.g., SEM, XPS, or Raman spectroscopy) to be carried out and enables the postprocessing of the gallenene-graphene heterostack for preparing further experiments. The propagation velocity of gallenene decreased with progressing time, and it took a few hours until the lower sample side was intercalated entirely [Fig. 1(a), II-III]. The total coverage of the top half, however, was completed only after a few days by storage of the sample at room temperature [Fig. 1(a), III–IV]. The initiation of self-propagation of gallenene on the SiC substrate is decisively influenced by temperature as a crucial parameter. So far, implementing this approach entirely at room temperature without heating at the initial stage has not led to the fabrication of gallenene films with such large dimensions.

B. Chemical characterization of gallenene

The formation and composition of a thin Ga film as metallene have been analyzed employing LA-ICP-MS and XPS, as shown in Fig. 2. In analytical chemistry, LA-ICP-MS has evolved to a standard technique that can be used to identify and quantify inorganic impurities, for instance in semiconductor materials [34–37]. Moreover, LA-ICP-MS mappings enable the lateral composition of thin films to be analyzed. Here, LA-ICP-MS mappings were measured over an area of $(80 \times 220)\,\mu\text{m}^2$ and with an increment as well as a laser spot size of 20 μm encompassing the sharp transition from gallenene (bright-colored area) to pure epitaxial graphene (dark-colored area) as shown in Figs. 2(a) (red-colored box) and 2(b). For better visualization, the pixels in Fig. 2(b) were linearly interpolated. The corresponding mass spectrum shows the signals of the two stable isotopes ^{69}Ga and ^{71}Ga [Fig. 2(c)] with small fractions of these isotopes, even occurring on pure epitaxial graphene, probably due to surface contaminations [red mass spectrum, Fig. 2(c)]. However, an

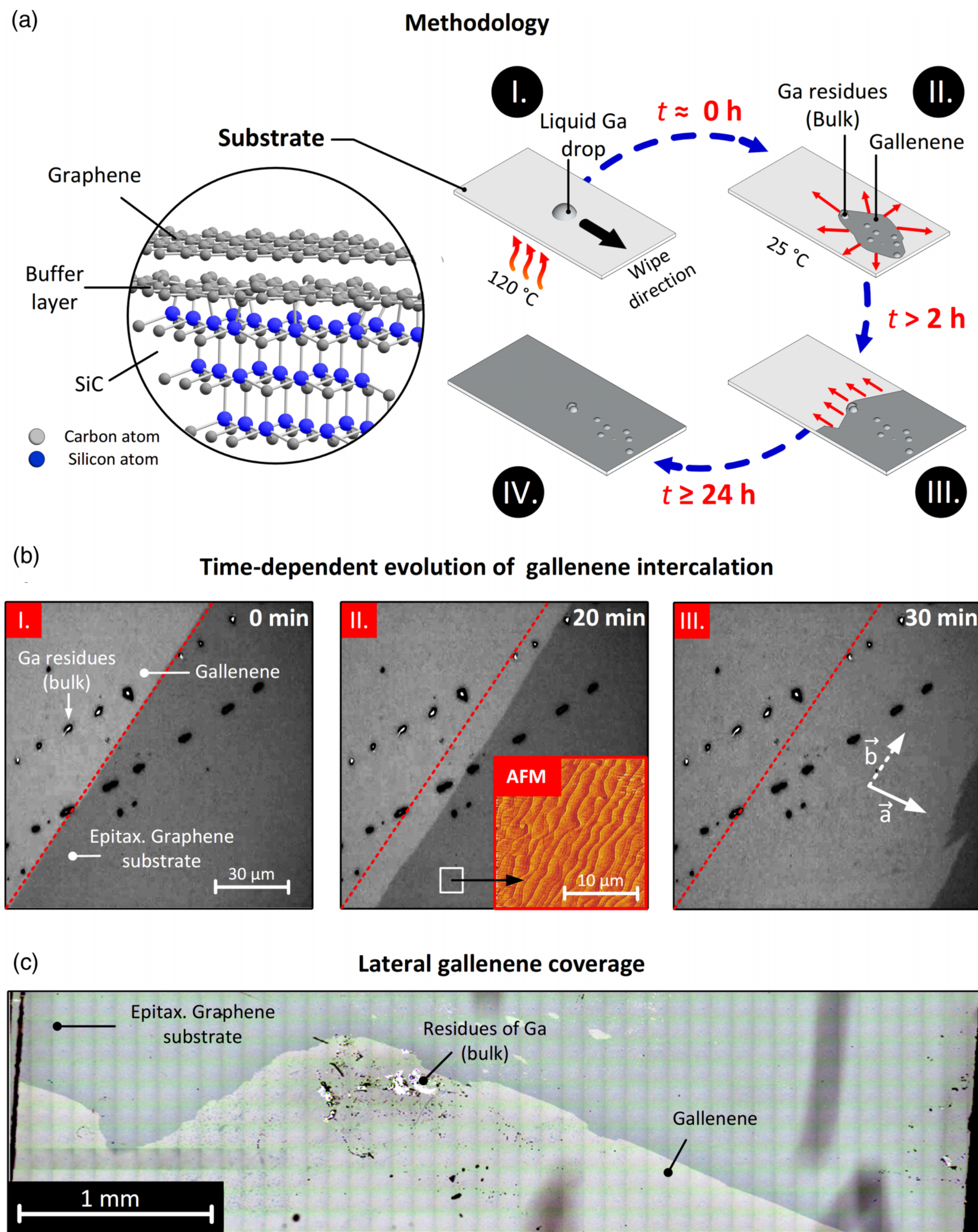

FIG. 1. (a) Schematic representation of gallenene self-propagation caused by the liquid metal intercalation technique (LiMIT). I. Initiation of the process by liquid Ga deposition and wiping the metal across the substrate. The inset shows schematically the sample structure consisting of a monolayer graphene sheet on top of a graphene buffer layer that is covalently bonded to the underlying SiC substrate. II. Self-propagation of gallenene shortly after processing. III. Self-propagation of gallenene after 2 h. IV. Gallenene completely intercalating the epitaxial graphene sample after >24 h. (b) I. Time-dependent self-propagation of gallenene. The red dashed line is used as a start marker. II. Time-dependent self-propagation of gallenene after 20 min. The inset indicates the terrace orientation of SiC steps measured with AFM on a pure epitaxial graphene surface. III. Time-dependent self-propagation of gallenene after 30 min. Vectors **a** and **b** indicate the self-propagation direction of Ga derived from AFM measurements. (c) Optical micrograph of the Ga intercalated graphene.

increase in the Ga signal by more than one order of magnitude appearing in brightly colored areas [red mass spectrum, Fig. 2(c)] undoubtedly demonstrates the presence of Ga on the substrate.

The chemical bonding states of graphene and gallenene have been studied by XPS, and their physical interactions with each other have been studied by XPS and Raman spectroscopy. Results from the latter technique will be discussed later. The upper XPS spectrum in Fig. 2(d) shows the superposition of carbon-carbon bond energies in epitaxial graphene, indicating the presence of graphene buffer layer, graphene (284.61 eV), and SiC substrate (283.72 eV) at C 1s core level [38]. Here, the binding energy of the graphene buffer layer is decomposed into S_1 (284.95 eV) and S_2 (285.54 eV) components, and it mimics various chemical bonding states within the graphene buffer layer [30,38,39], which, in turn,

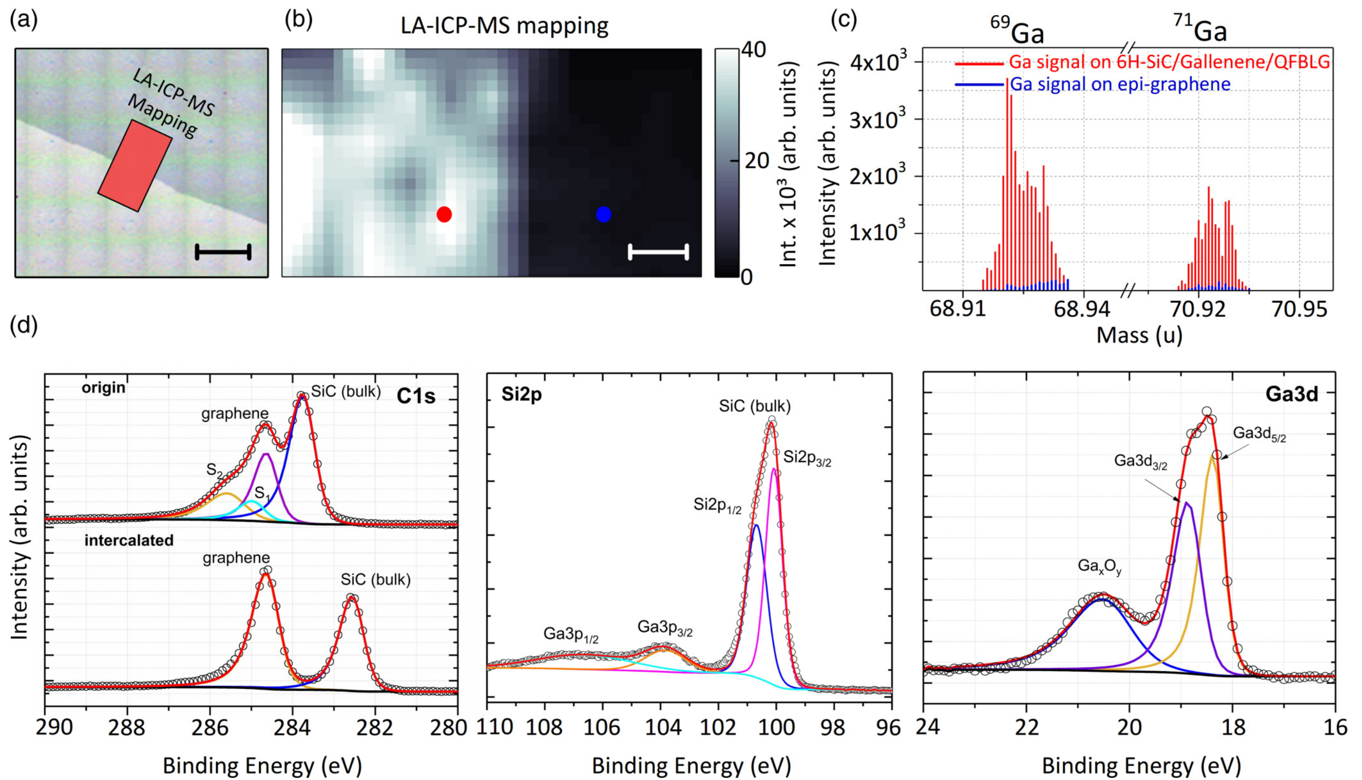

FIG. 2. (a) Optical micrograph of the area considered for the LA-ICP-MS measurements. Scale bar corresponds to a width of 100 μm. (b) False color mapping across the transition of nonintercalated epitaxial graphene to Ga-intercalated graphene using LA-ICP-MS. Scale bar corresponds to a width of 20 μm. (c) Mass spectrum of pure epitaxial graphene (blue) and Ga-intercalated graphene (red), showing signal intensities of gallium isotopes ^{69}Ga and ^{71}Ga. Both spectra result from areas from LA-ICP-MS mapping (marked with a blue and red circle). (d) XPS spectra of the C 1s and Si 2p core-level before and after Ga intercalation of epitaxial graphene. Ga 3d core-level demonstrating the presence of elemental Ga as well as Ga-oxide contents.

belong to chemical bonds between the buffer layer and the Si-face of the substrate [30,38–40]. Upon Ga deposition, the two signals S_1 and S_2 vanish, leaving only the binding energies of graphene and the substrate. The same XPS features have been observed by Briggs *et al.* [28] and in the intercalation process of epitaxial monolayer graphene in different gas atmospheres resulting in a transformation into QFBLG [38]. In the latter case, at elevated temperatures, the gas molecules break the chemical bonds between the graphene buffer layer and the substrate and passivate at the same time the dangling bonds on the Si-face during the intercalation process [39–41]. As can be seen from XPS measurements, the Ga 3d core-level spectrum reveals Ga-Ga bonding states in gallenene at ~18.5 eV [42]. The metallic phase of gallenene is furthermore accompanied by small gallium oxide fractions at 20.49 eV [43]. Comparable oxide signals have been measured on top of the intercalated graphene bilayer by Briggs *et al.* [28], where a high-temperature approach in the vacuum has been employed. In contrast, we assume that small fractions of the gallium oxide are intercalated beneath epitaxial graphene since LiMIT was carried out at an ambient atmosphere. More importantly, such oxide signals were explicitly measured in areas that were free of Ga contamination of the graphene upper surface resulting only from the liquid metal intercalation. Additional signals in the Si 2p core-level spectrum at ~103.8 and ~106.7 eV can be assigned to the Ga 3p binding energies with spin $^1/_2$ and $^3/_2$ [42].

Using angle-resolved XPS measurements (ARXPS), attempts were made to detect possible evidence of bonding states of Si-Ga in the binding energy range near ~1116 eV of the Ga 2p core level [44] as well as in the binding energy range around ~19 eV of the Ga 3d core-level spectrum [45]. Si-O bonding states at the gallenene-SiC interface have been investigated in the Si 2p core-level spectrum at 103 eV [41,46,47]. The first state indicates binding energies between gallenene and the Si-face of the substrate, and the latter indicates a thin silicon oxide layer at the gallenene to substrate interface resulting from the presence of oxygen in oxidized gallenene [Fig. 2(d), Ga 3d core level]. However, our measurements show no such bonding states between Si-Ga and Si-O, since these, if any, are below the detection limit of the XPS measurement. From that, we suggest that not only is Ga responsible for the intercalation process, but additionally a small fraction of oxygen might also saturate some dangling bonds on the Si-face [46,47]. Therefore, both Ga and oxygen must be taken into account here. Nevertheless, XPS clearly shows the complete conversion of epitaxial graphene into QFBLG and thus underpins that the existing dangling bonds could be crucial for the intercalation, as has already been shown in the literature. We would like to point out that supercooled liquid Ga also has

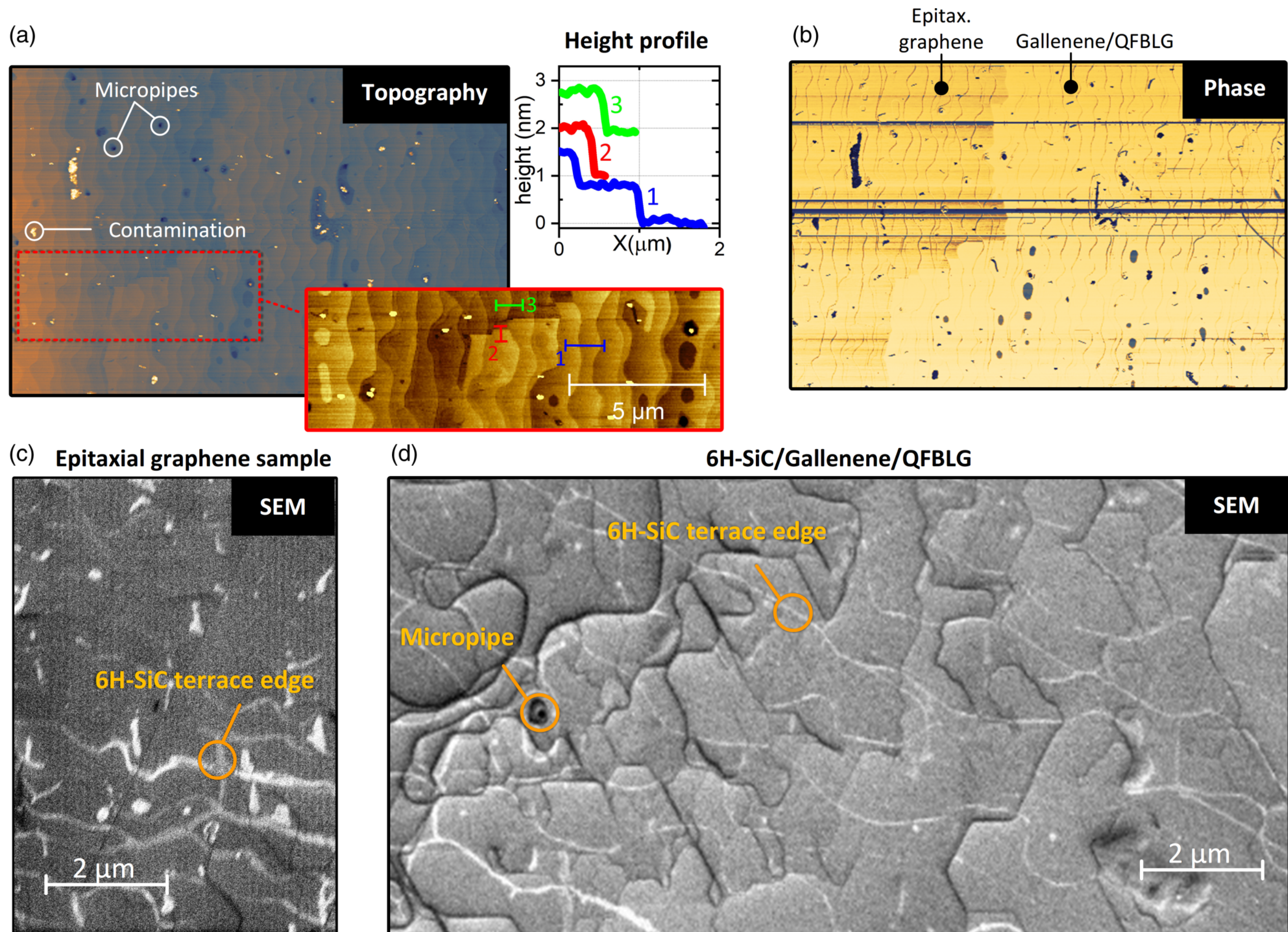

FIG. 3. (a) and (b) AFM topography and phase image of gallenene on epitaxial graphene. The inset shows a magnified representation of the measured topography (red dashed box), specifically the transition from epitaxial graphene substrate to gallenene covered areas. The line profile extracted from the topography (blue, red, and green line) represents the thickness of gallenene (red) measured at the intercalated/nonintercalated border, the step height of the terraces (green), and the thickness of Ga film across a gallenene area (blue). (c) and (d) Scanning electron microscopy image (at 2 keV) of epitaxial graphene and a Ga intercalated graphene area measured with an in-beam mode SEM image. White stripes indicate terrace edges of SiC.

an anomalous physical behavior, which could be an essential criterion for intercalation at room temperature, which will be discussed later.

The topological structure and coverage of gallenene across the substrate was also characterized by AFM and SEM (Fig. 3). Figure 3(a) shows the SiC substrate's topography, including the typical terrace structure, as already shown in the previous section on the pure epitaxial graphene surface. The topography image also shows a high density of small holelike defects on the substrate, also known as micropipes. Larger areas covered with micropipes across epitaxial graphene samples were recorded by SEM and can be found in the supplemental material (Fig. S2) [33]. These surface defects occur in low crystal quality SiC wafers, or they could have been created during graphene fabrication employing the PASG process. The origin of the micropipes can be theoretically described by the Frank theory, according to which they often appear due to the bunching of several screw dislocations to a superscrew dislocation [48]. In addition, the growth of epitaxial graphene stops at dislocations, and, under certain circumstances, these defects develop into patches of bilayer or even few-layer graphene [49]. The identification of the deposited gallenene sheets from AFM topography images is challenging because the measured gallenene topography is disturbed by the dominant SiC terraces. On the other hand, the AFM phase contrast image readily shows changes in the material properties, thus enabling the identification of pure epitaxial graphene and gallenene [Fig. 3(b)]. A sharp transition boundary between areas of pure epitaxial graphene and large gallenene areas appears as a slight contrast change in the phase image [Fig. 3(b)]. The difference in height between the pure substrate and the Ga intercalated areas is particularly evident, along with the terrace steps of the substrate [Fig. 3(a), inset—red box]. The average thickness of gallenene of about 1 nm can be observed in these areas [Fig. 3(a), line profile—line no. 2, red line], which is approximately four times smaller compared to the value of the solid-melt exfoliation approach of liquid Ga on Si(111) [17]. In contrast, the green line (line no. 3) shows an average terrace height of 6H-SiC of about 0.75 nm. In comparison to high-resolution TEM measurements on

gallenene showing a range of Ga layer thickness of 2–3 [28], our AFM results of Ga layer thickness are in a quite similar range of three to four gallenene layers. The blue line (line no. 1) depicts the height profile on a Ga intercalated graphene area showing the same step height of 0.75 nm as on pure substrate and indicating a homogeneous layer thickness within the gallenene film. The layer thickness of Ga is related to the metal chemical potential as calculated from DFT calculations [28].

High-resolution in-beam SEM images [Figs. 3(c) and 3(d)] have been used to reveal the topological difference between gallenene-free [Fig. 3(c)] and gallenene-intercalated [Fig. 3(d)] areas of graphene on the SiC substrate. The presence of gallenene leads to a brighter contrast [Fig. 3(d)] compared to the pure epitaxial graphene region [Fig. 3(c)]. The SEM images also reveal the well-resolved characteristic terrace steps of the SiC wafer depicted as bright lines (white stripes) along the characteristic SiC terrace step edges, which remain visible even throughout the gallenene film [Figs. 3(c) and 3(d)]. Additionally, various dark lines appear within the gallenene film [Fig. 3(d)]. These lines clearly point out a symmetrical shape that could be forced by the hexagonal symmetry of the Si-face and indicate grain boundaries within the gallenene film, which is in good agreement with Raman measurements discussed below. It is worthwhile to mention that an interesting reflectivity contrast is also observed in the SEM imaging of the SiC/Ga/BLG heterostack on the nonidentical SiC terraces, which can be related to the stacking-order-induced doping valuation from the 6H-SiC stacking terminations [50].

C. Investigation of transition from epitaxial graphene to QFBLG using Raman spectroscopy

Raman spectroscopy is an essential instrument for characterizing 2D materials and is used here to investigate the lattice structure and interactions between graphene and gallenene on the micrometer scale. Raman spectra from pure epitaxial graphene (black line) and the gallenene-intercalated graphene area on 6H-SiC (SiC/Ga/QFBLG, red line) are depicted in Fig. 4(a). Both Raman spectra contain phonon bands that belong to the SiC substrate (marked with an asterisk). Characteristic phonon bands of graphene appear at 1580 and 2670 cm^{-1}, corresponding to the well-known G and 2D peak. The physical origin of the D, G, and 2D peak of graphene has been extensively investigated, and a description can be found elsewhere [51–55]. The Raman spectrum of gallenene-intercalated areas [Fig. 4(a), red line] exhibits a strong signal between 45 and 750 cm^{-1}, with its maximum occurring at $\sim$104 cm^{-1} compared to the Raman spectrum of the pure epitaxial graphene substrate [black line, Fig. 4(a)]. However, the gallenene spectrum is not completely visible in the low-wave-number range >45 cm^{-1} as these bands have been cut by a holographic edge filter placed in the optical path of the spectrometer [Fig. 4(a), red line].

Figure 4(b) depicts the subtracted Raman spectra of pure epitaxial graphene (black line) as well as of the gallenene-graphene heterostack (red line) from a reference spectrum obtained from pure 6H-SiC especially to reveal the graphene buffer layer spectrum, which is normally superimposed by the second-order overtone of SiC. The Raman spectrum of the graphene buffer layer (BL) in epitaxial graphene occurs as flat and broadened phonon bands in the Raman spectral range from 1200 to 1600 cm^{-1} [56]. The BL background vanishes on gallenene-intercalated graphene areas, as shown in Fig. 4(b) (red line), followed by an increase of the G peak intensity. Furthermore, the 2D peak line shape changes in gallenene-intercalated areas, as depicted in Fig. 4(c) (red line), and it can be fitted by four Lorentzian curves, which is typical for bilayer graphene (for more details, see Fig. S3 in the supplemental material) [33]. All mentioned Raman spectral changes occurring in the change of epitaxial graphene are typical for the intercalation process and transition of epitaxial graphene to QFBLG. Detailed studies on the intercalation of epitaxial graphene using gases (e.g., hydrogen, oxygen) have been extensively investigated and can be found elsewhere [44–46]. The characteristic low-energy out-of-plane phonon modes (around 100 and 1800 cm^{-1}) of bilayer graphene [57] as another important feature are superimposed by the background signal of gallenene and the second-order vibrational modes of SiC, and they were therefore not observed in our Raman measurements. The time-dependent evolution of the transition from epitaxial graphene to QFBLG during the Ga self-propagation has been measured to examine the dynamical spectral change of the epitaxial graphene Raman spectrum during the self-propagation process of Ga and is represented in Fig. 4(d). The intensity of the G and the 2D peak widens instantly as the Ga signal rises showing that the intercalation and thus the transition from epitaxial graphene to QFBLG does not occur without the presence of Ga.

The lateral distribution of the individual graphene and gallenene phonon bands was measured using microconfocal Raman mappings in combination with an automated nonlinear fitting algorithm that extracts the characteristic parameters such as peak position and peak width [Figs. 5(b)–5(d)]. All Raman spectra were corrected by subtracting a reference spectrum obtained from pure 6H-SiC since the second-order vibrational modes of 6H-SiC cover the Raman spectrum of graphene in a spectral range between 1200 and 2000 cm^{-1}, leading to a spectral superposition.

An optical micrograph of the investigated area along the transition border of the nonintercalated and intercalated area is shown in Fig. 5(a). The Raman mapping in Fig. 5(b) depicts the collected intensity distribution of gallenene across the epitaxial graphene. Black areas reveal the absence of gallenene, showing nonintercalated epitaxial graphene, whereas green regions indicate the rise of the gallenene background signal in the Raman spectrum. The false-color image of the 2D peak width distribution in Fig. 5(c) illustrates a distinct contrast difference, representing a broadening of the 2D peak width on gallenene intercalate areas, which is consistent with the gallenene background signal distribution in Fig. 5(b). A statistical evaluation of the 2D peak width of Fig. 5(c) underpins this effect by the formation of two separated Gaussian-like distributions [histogram, Fig. 5(f)] with the 2D peak widths being (34.7 ± 5.3) and (53.9 ± 9.1) cm^{-1}. The former distribution denotes 2D peak widths typically measured for epitaxially grown monolayer graphene [58], while the latter indicates bilayer graphene.

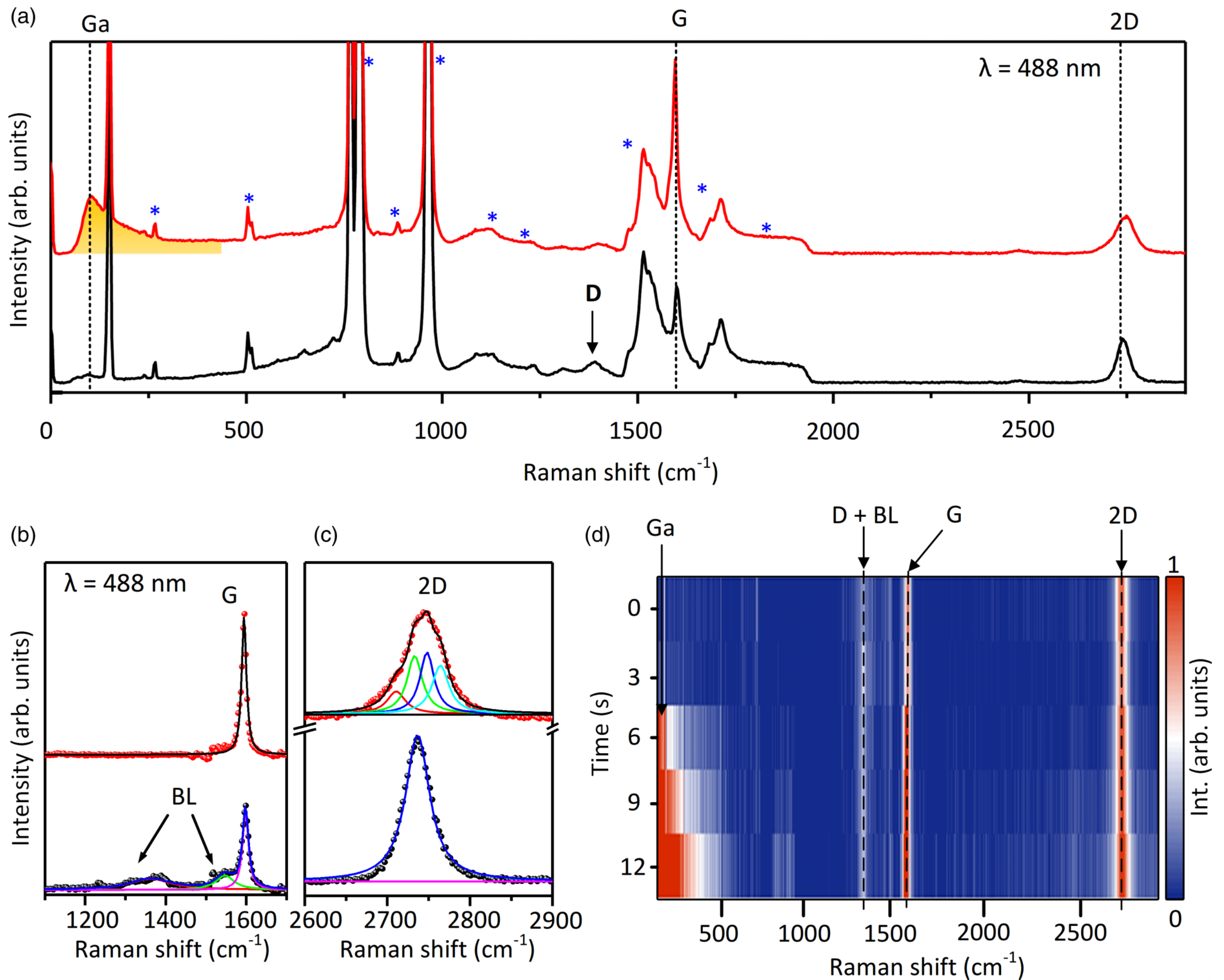

FIG. 4. (a) Raman spectra of pure epitaxial graphene (black line) and intercalated area consisting of SiC/Ga/QFBLG (red line). The Raman signal related to gallenene appears below 250 cm^{-1} (dashed purple line). SiC phonon bands are marked with an asterisk. (b) and (c) Subtracted Raman spectrum of epitaxial graphene (blue line) and intercalated QFBLG (red line). (d) Time-dependent evolution of the phonon bands of graphene during the gallenene self-propagation. The intercalation of epitaxial graphene to QFBLG appears after 6 s.

D. Microstructural order of gallenene

Creighton and Withnall have analyzed the space-group symmetry of α-Ga, whereupon four Ga atoms occupy the primitive unit cell of a D_{2h}^{18} space group, and thus they result in six Raman-active phonon bands of α-Ga [20]. Their Raman spectroscopic experiments have shown that only one characteristic Raman band of solid α-Ga appears around 246 cm^{-1}, corresponding to the symmetrical stretching of Ga pairs. No such phonon band appeared in the Raman spectra of gallenene [Fig. 4(a), red line], most likely due to a structural change of the gallenene lattice compared to the α-Ga (bulk) resulting from the confinement at the graphene–6H-SiC interface as observed by Briggs *et al.* using TEM [28]. There it is suggested that trilayer gallenene arises along the hexagonal lattice plane (111) of a distorted face-centered-cubic (fcc) crystal symmetry of Ga(III) phase under high pressure between graphene and the hexagonal lattice plane (0001) of SiC substrate. Interestingly, Steenbergen *et al.* have calculated a new phase of trilayer gallenene structure using DFT calculations [59], which is comparable to the lattice structure of the beta phase of bulk Ga. The calculated trilayer structure occupies the same hexagonal lattice symmetry as the Si-face of SiC substrate, and from our point of view this indicates a low lattice mismatch between both materials. In particular, the cross-sectional side view of the calculated trilayer gallenene crystal lattice resembles well the cross-sectional TEM measurements given in the literature [28], and it could therefore be an alternative model to the suggested Ga(III) phase [28].

This spectral shape closely resembles that of a boson peak, which is a typical effect arising in supercooled liquids [60] or highly polycrystalline or amorphous materials [61]. Raman spectroscopic investigations of bulk Ga droplets have revealed a similar spectral line shape as compared to gallenene (Fig. S4 in the Supplemental Material) [33] that was already observed by Lee and Kang even on thin β-Ga_2O_3 films [62]. In

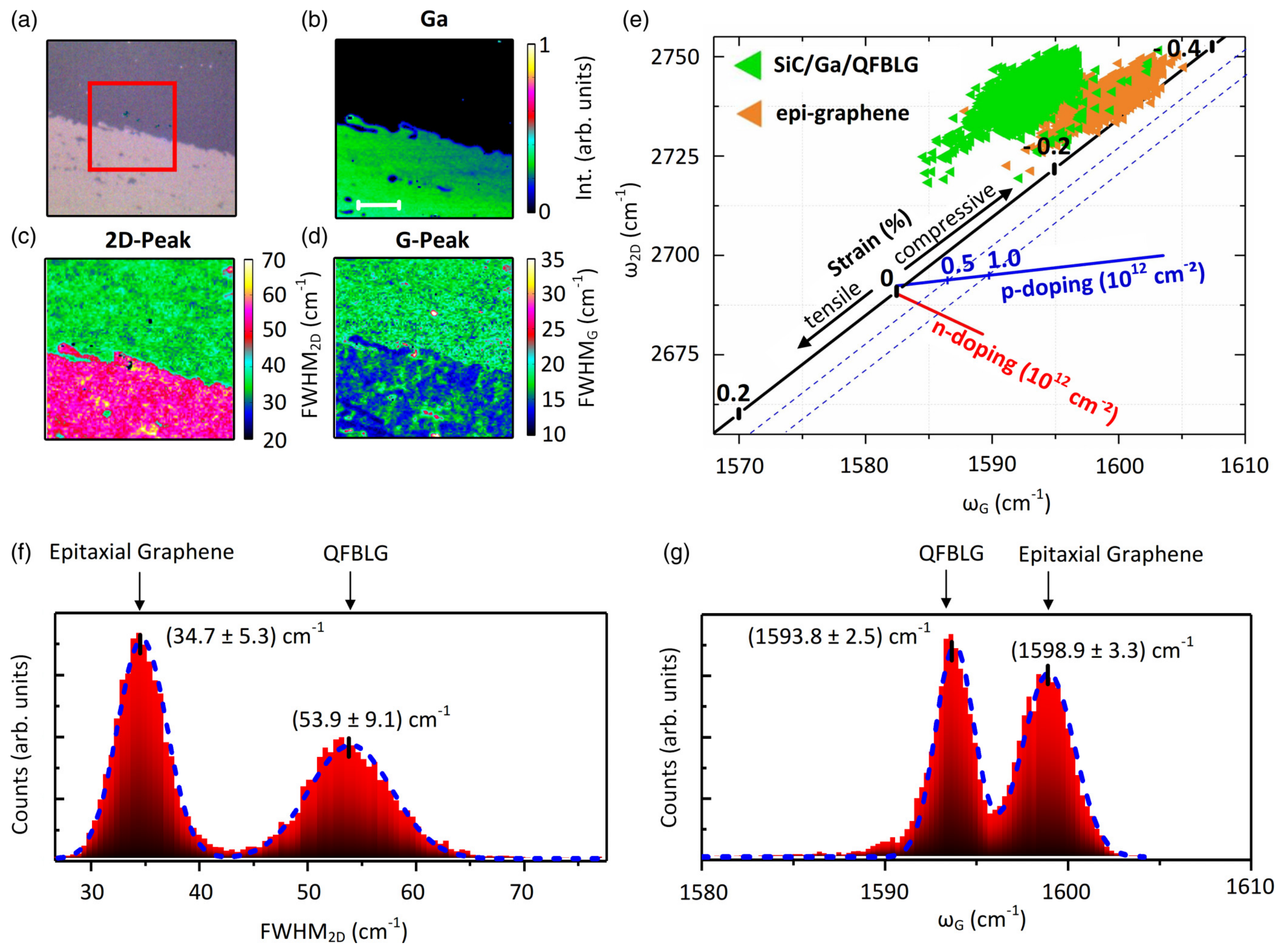

FIG. 5. (a) Optical micrograph of the gallene-graphene boundary indicating the area selected for Raman mapping (red square). (b) Measured Raman intensity signal of gallenene. Dark areas represent areas of pure epitaxial graphene substrate. Green areas correspond to gallenene (c) Lateral 2D peak width distribution along the graphene-gallenene boundary. Green areas indicate regions of monolayer epitaxial graphene, whereas pink areas indicate the intercalation of epitaxial graphene caused by gallenene. The scale bar corresponds to a width of 5 μm. (d) G peak width distribution indicating electronic doping within graphene on gallenene-covered areas (blue areas). (e) Strain-doping trajectory of epitaxial graphene (yellow dots) and intercalated QFBLG (green dots). (f) Histogram of the 2D peak width of epitaxial graphene and intercalated QFBLG extracted from Raman mapping. (g) Histogram of the G peak position width of epitaxial graphene and intercalated QFBLG extracted from Raman mapping.

their work, the growth mechanism of β-Ga_2O_3 nanowires on amorphous substrates using an RF powder-sputtering method has been analyzed by several analytical tools, including Raman spectroscopy. Lee and Kang have shown that the typical characteristic phonon bands belong to the monocrystalline crystal structure of β-Ga_2O_3, but they also observed two broadened bands at 115 and 703 cm^{-1} on thin Ga films. Based on their Raman data, they suggested that a low crystallinity phase exists in those thin films, which cannot be assigned to known Raman-active phonon modes of pure solid Ga or β-Ga_2O_3, but might instead indicate the presence of a Ga-rich oxide phase [62]. Hence, their data support our experimental results of micro-Raman and XPS measurements, indicating a low-crystalline gallenene phase to be formed after the deposition onto the SiC substrate when using the solid-liquid exfoliation-intercalation technique. Furthermore, the Raman results support our SEM measurements indicating grain boundaries of gallenene at the micrometer scale. It is also expected that supercooled Ga exhibits an anomalous liquid behavior at specific temperature and pressure conditions [63]. The anomaly manifests itself as a density anomaly occurring as liquid phase separation, also called a low-density liquid (LDL) and a high-density liquid (HDL), and as a thermodynamic anomaly. The change of liquid density of the supercooled Ga phase could support the intercalation process and the existing driving force of dangling bonds [28], which could act as a capillary force for Ga atoms. The change of liquid density of supercooled Ga might increase the mobility of Ga atoms, which thus enables a higher diffusion length of Ga atoms beneath epitaxial graphene, so a metastable liquid state of Ga arises under these conditions. The Raman spectroscopic investigations of gallenene instead suggest a nanocrystalline phase or possibly even the presence of a metastable liquid phase of Ga at the microscale. A similar signal seems to appear in the Raman spectra of Kochat *et al.*, showing the spectral fingerprint of pure gallenene and the gallenene-MoS_2

heterostack [17]. Unfortunately, a description of this signal is missing in their work. Overall, considering our measurements and the current literature, some questions about the gallenene lattice structure at the Si/graphene interface remain, so that further measurements have to be carried out for clarification.

E. Interlayer interactions of a graphene-gallenene heterostack

The charge-carrier doping and physical interactions resulting in strain between gallenene and graphene were evaluated using confocal micro-Raman spectroscopy and van der Pauw (VdP) measurements [64–69]. Charge-carrier doping in graphene significantly affects its Raman spectroscopic properties by changing the G peak position and peak width, typically resulting in stiffening and sharpening of the G peak [64,66]. Figure 5(d) depicts the G peak width mapping of graphene, indicating predominantly blue and green areas corresponding to G peak widths of 12 and 16 cm^{-1}. While the green areas indicate the absence of carrier doping in epitaxial graphene, the blue regions correspond to slight carrier doping of approximately $5 \times 10^{12}\,cm^{-2}$ [66] introduced due to the interaction with gallenene, finally changing the carrier density of bilayer graphene. Furthermore, carrier doping occurs only on gallenene-intercalated areas and is delimited by a sharp border, as shown in Fig. 5(d). In addition, Fig. 5(d) depicts a nonhomogeneous distribution of the G peak width on gallenene-intercalated areas, which implies rather heterogeneous doping across the graphene-gallenene heterostack.

Due to this effect, VdP measurements have been carried out to calculate the carrier density (n or$p$) and carrier mobility (μ) as a function of temperature in the sample [70]. The VdP measurement was performed without applying any lithography processing on the samples. The VdP measurement setup and sample preparation can be found in Ref. [31]. The low carrier mobility of $\mu \approx (300 \pm 50)\,cm^2\,V^{-1}\,s^{-1}$ as well as strong electron doping of $n \approx (4.5 \pm 0.1) \times 10^{12}\,cm^{-2}$ and a sheet resistance $R_s \approx (4500 \pm 50)\,\Omega$ have been measured on SiC–gallenene–QFBLG samples (SiC/Ga/QFBLG). This lower mobility is mainly due to the temperature-dependent electron-phonon scattering that prevails at higher temperatures. Thereby, $n \approx (1.3 \pm 0.1) \times 10^{12}\,cm^{-2}$, $\mu \approx (1350 \pm 50)\,cm^2\,V^{-1}\,s^{-1}$, and $R_s \approx (3700 \pm 50)\,\Omega$ are calculated at cryogenic temperatures ($T = 4.5\,K$). Here, the n-doping is a superposition of the carriers induced by both SiC and gallenene that make the free-standing top graphene bilayer n-type but not p-type, as would be the case, for example, by hydrogen intercalation [31,71]. In addition, the SiC/Ga/QFBLG sample shows much lower mobility both at room temperature and at low temperatures compared to the QFBLG sample prepared using hydrogen intercalation in the same VdP regime, $\mu \approx 2700\,cm^2\,V^{-1}\,s^{-1}$ ($T = 295\,K$) and $\mu \approx 3350\,cm^2\,V^{-1}\,s^{-1}$ ($T = 2.2\,K$) [31], indicating a higher charge-carrier scattering in the SiC/Ga/QFBLG system. Such strong electron doping concentration could be relevant for plasmonic applications such as substrates for surface-enhanced and tip-enhanced Raman spectroscopy (SERS and TERS) or tip-enhanced photoluminescence spectroscopy (TEPL). In this context, the optical properties of gallenene have been investigated using other optical techniques, and they are available in the supplemental material (Fig. S5) [33], but they are not the subject of discussion in this article.

The strain level within the graphene crystal lattice can be significantly affected by the intercalation process [41]. In this context, we have noticed a shift of the G peak position from $(1598.9 \pm 3.3)\,cm^{-1}$ down to $(1593.8 \pm 2.5)\,cm^{-1}$ [Fig. 5(g)], indicating a slight reduction of the strain level. Nevertheless, the G peak position is also superimposed by electronic doping [72], as has already been proved by the reduced G peak width. A more detailed analysis by using a strain-doping trajectory [68] for the G and 2D peak has shown that compressive strain in epitaxial graphene of $\varepsilon \sim 0.3$ is slightly decreased down to $\varepsilon \sim 0.2$ in QFBLG after the Ga intercalation. However, these experimental findings cannot be confirmed by literature data since an extensive study of the strain-doping trajectory for bilayer graphene is still missing. The trajectory shown in Fig. 5(e) has been taken from previous work, as explained elsewhere [41]. The remaining compressive strain within graphene indicates strong interactions between gallenene and graphene layers. This can be expected since Ga atoms of gallenene seem to be arranged in a similar hexagonal symmetry to SiC (0001), resulting in a lattice mismatch between graphene and gallenene. Additionally, further mechanical strain in graphene is also introduced at the transition border from QFBLG to epitaxial graphene resulting from inhomogeneous Ga intercalation below graphene [see Figs. 5(a)–5(c)].

Ga intercalated graphene areas have also been examined to defect densities within a graphene lattice that could be introduced by Ga intercalation or by the sample preparation procedure. The Raman spectral investigations of the Ga intercalated graphene areas do not reveal any increased defect density of graphene after the gallenene spreading (see Fig. S6 in the supplemental material) [33], proving the advantage of using micropipes within the SiC substrate and corresponding holes in graphene for epitaxial graphene intercalation. Ga intercalation through highly defective epitaxial graphene, which was pretreated by plasma etching, is followed by the "self-healing" of the graphene lattice, reducing the defect density. However, the Raman spectra of Briggs *et al.* indicate that small defect densities remain after the self-healing process, suggesting a slightly reduced crystal quality of QFBLG [28]. It can be concluded that defect density engineering of epitaxial graphene is a critical technology for creating high-quality heterostructures through intercalation. Al Balushi *et al.* demonstrated that graphene wrinkles enhance the nucleation process of Ga [27]. Other research groups have shown that the infiltration of alkali atoms can be achieved through wrinkles, which act as penetration sides [73]. In our case, the microholes present in both graphene and SiC act as nucleation centers for Ga atoms due to a decreased surface energy, and they support the intercalation of Ga atoms by enabling them to get under the buffer layer.

IV. CONCLUSIONS

In summary, we have demonstrated an alternative approach to fabricate a large-area gallenene layer through the intercalation of liquid metal beneath epitaxial graphene at ambient

conditions by self-propagation and diffusion of Ga atoms at room temperature. Our measurement results suggest that liquid Ga penetrates through substrate defects of SiC, such as micropipes, and it intercalates the graphene buffer layer, which finally converts the epitaxial graphene into QFBLG, as demonstrated by XPS and confocal micro-Raman spectroscopy. Furthermore, we assume that the resulting gallenene film at the graphene-SiC interface has rather nanocrystalline properties and is in a metastable state.

The self-organized process of Ga diffusion beneath epitaxial graphene can be realized at low temperature enabling the *in situ* characterization of epitaxial graphene intercalation even at room temperature. Clusters of hollow defects, in the form of micropipes in 6H-SiC in the present work, triggered the diffusion of Ga atoms of gallenene. The self-propagation of Ga is energetically favored along the SiC terrace, whereas the terrace steps form an energetic barrier (Ehrlich-Schwoebel barrier) as revealed by optical microscopy and AFM, retarding the gallenene propagation. We propose that dangling bonds at the SiC–buffer-layer interface trigger the intercalation process of Ga along the Si-face of 6H-SiC, which might also be supported by the liquid-liquid-phase transition of Ga at high pressure between the graphene/SiC interface. Symmetrical shapes within the gallenene film have been observed using SEM, which could be related to domain borders or grain boundaries forced by the hexagonal lattice symmetry (0001) of the Si-face of the 6H-SiC.

The presented liquid metal intercalation technique (LiMIT), combined with large-area epitaxial monolayer graphene sheets, might be able to open a new route toward a controlled fabrication of homogeneous large-area metallene layers employing liquid metals. The intercalated metallenes (based on Ga, In, Sn, etc.) at the graphene-SiC interface allow possibly the conversion into corresponding semiconductor derivatives such as an oxide or nitride layer enabling new types of semiconductor devices.

ACKNOWLEDGMENTS

S.W. acknowledges support from the Braunschweig International Graduate School of Metrology B-IGSM. D.M. acknowledges support from the school for contacts in nanosystems (NTH). The work has received funding from the European Metrology Programme for Innovation and Research (EMPIR) under Grant No. 17FUN08 cofinanced by the Participating States and from the European Union's Horizon 2020 research and innovation program. The work was also cofunded by the Deutsche Forschungsgemeinschaft (DFG) under Germany's Excellence Strategy–EXC-2123 Quantum Frontiers (390837967).

[1] Y. Gong, S. Lei, G. Ye, B. Li, Y. He, K. Keyshar, X. Zhang, Q. Wang, J. Lou, Z. Liu, R. Vajtai, W. Zhou, and P. M. Ajayan, Nano Lett. **15**, 6135 (2015).

[2] G. W. Shim, K. Yoo, S. B. Seo, J. Shin, D. Y. Jung, I. S. Kang, C. W. Ahn, B. J. Cho, and S. Y. Choi, ACS Nano **8**, 6655 (2014).

[3] C. Huang, S. Wu, A. M. Sanchez, J. J. P. Peters, R. Beanland, J. S. Ross, P. Rivera, W. Yao, D. H. Cobden, and X. Xu, Nat. Mater. **13**, 1096 (2014).

[4] W. T. Hsu, Z. A. Zhao, L. J. Li, C. H. Chen, M. H. Chiu, P. S. Chang, Y. C. Chou, and W. H. Chang, ACS Nano **8**, 2951 (2014).

[5] Y. Gong, J. Lin, X. Wang, G. Shi, S. Lei, Z. Lin, X. Zou, G. Ye, R. Vajtai, B. I. Yakobson, H. Terrones, M. Terrones, B. K. Tay, J. Lou, S. T. Pantelides, Z. Liu, W. Zhou, and P. M. Ajayan, Nat. Mater. **13**, 1135 (2014).

[6] X. Duan, C. Wang, J. C. Shaw, R. Cheng, Y. Chen, H. Li, X. Wu, Y. Tang, Q. Zhang, A. Pan, J. Jiang, R. Yu, Y. Huang, and X. Duan, Nat. Nanotechnol. **9**, 1024 (2014).

[7] Y. Shi, W. Zhou, A. Y. Lu, W. Fang, Y. H. Lee, A. L. Hsu, S. M. Kim, K. K. Kim, H. Y. Yang, L. J. Li, J. C. Idrobo, and J. Kong, Nano Lett. **12**, 2784 (2012).

[8] S. J. Haigh, A. Gholinia, R. Jalil, S. Romani, L. Britnell, D. C. Elias, K. S. Novoselov, L. A. Ponomarenko, A. K. Geim, and R. Gorbachev, Nat. Mater. **11**, 764 (2012).

[9] L. Britnell, R. V. Gorbachev, R. Jalil, B. D. Belle, F. Schedin, A. Mishchenko, T. Georgiou, M. I. Katsnelson, L. Eaves, S. V. Morozov, N. M. R. Peres, J. Leist, A. K. Geim, K. S. Novoselov, and L. A. Ponomarenko, Science **335**, 947 (2012).

[10] K. S. Novoselov, A. K. Geim, S. V. Morozov, D. Jiang, Y. Zhang, S. V. Dubonos, I. V. Grigorieva, and A. A. Firsov, Science **306**, 666 (2004).

[11] X. Geng, W. Sun, W. Wu, B. Chen, A. Al-Hilo, M. Benamara, H. Zhu, F. Watanabe, J. Cui, and T. P. Chen, Nat. Commun. **7**, 10672 (2016).

[12] J. Shen, Y. He, J. Wu, C. Gao, K. Keyshar, X. Zhang, Y. Yang, M. Ye, R. Vajtai, J. Lou, and P. M. Ajayan, Nano Lett. **15**, 5449 (2015).

[13] J. Zheng, H. Zhang, S. Dong, Y. Liu, C. Tai Nai, H. Suk Shin, H. Young Jeong, B. Liu, and K. Ping Loh, Nat. Commun. **5**, 2995 (2014).

[14] G. Z. Magda, J. Petõ, G. Dobrik, C. Hwang, L. P. Biró, and L. Tapasztó, Sci. Rep. **5**, 3 (2015).

[15] M. W. Iqbal, M. Z. Iqbal, M. F. Khan, M. A. Shehzad, Y. Seo, J. H. Park, C. Hwang, and J. Eom, Sci. Rep. **5**, 10699 (2015).

[16] A. Falin, Q. Cai, E. J. G. Santos, D. Scullion, D. Qian, R. Zhang, Z. Yang, S. Huang, K. Watanabe, T. Taniguchi, M. R. Barnett, Y. Chen, R. S. Ruoff, and L. H. Li, Nat. Commun. **8**, 15815 (2017).

[17] V. Kochat, A. Samanta, Y. Zhang, S. Bhowmick, P. Manimunda, S. A. S. Asif, A. S. Stender, R. Vajtai, A. K. Singh, C. S. Tiwary, and P. M. Ajayan, Sci. Adv. **4**, e1701373 (2018).

[18] P. Cheyssac, R. Kofman, and R. Garrigos, Solid State Commun. **44**, 1583 (1982).

[19] R. Kofman, P. Cheyssac, and J. Richard, Phys. Rev. B **16**, 5216 (1977).

[20] J. A. Creighton and R. Withnall, Chem. Phys. Lett. **326**, 311 (2000).

[21] L. Comez, A. Di Cicco, J. P. Itié, and A. Polian, Phys. Rev. B **65**, 014114 (2002).

[22] L. Bosio and C. G. Windsor, Phys. Rev. Lett. **35**, 1652 (1975).

[23] D. G. Carlson, J. Feder, and A. Segmüller, Phys. Rev. A **9**, 400 (1974).

[24] M. L. Tao, Y. B. Tu, K. Sun, Y. L. Wang, Z. B. Xie, L. Liu, M. X. Shi, and J. Z. Wang, 2D Mater. **5**, 035009 (2018).

[25] B. J. Carey, J. Z. Ou, R. M. Clark, K. J. Berean, A. Zavabeti, A. S. R. Chesman, S. P. Russo, D. W. M. Lau, Z. Q. Xu, Q. Bao, O. Kevehei, B. C. Gibson, M. D. Dickey, R. B. Kaner, T. Daeneke, and K. Kalantar-Zadeh, Nat. Commun. **8**, 14482 (2017).

[26] H. M. Zhang, Y. Sun, W. Li, J. P. Peng, C. L. Song, Y. Xing, Q. Zhang, J. Guan, Z. Li, Y. Zhao, S. Ji, L. Wang, K. He, X. Chen, L. Gu, L. Ling, M. Tian, L. Li, X. C. Xie, J. Liu, H. Yang, Q. K. Xue, J. Wang, and X. Ma, Phys. Rev. Lett. **114**, 107003 (2015).

[27] Z. Y. Al Balushi, K. Wang, R. K. Ghosh, R. A. Vilá, S. M. Eichfeld, J. D. Caldwell, X. Qin, Y. C. Lin, P. A. Desario, G. Stone, S. Subramanian, D. F. Paul, R. M. Wallace, S. Datta, J. M. Redwing, and J. A. Robinson, Nat. Mater. **15**, 1166 (2016).

[28] N. Briggs, B. Bersch, Y. Wang, J. Jiang, R. J. Koch, N. Nayir, K. Wang, M. Kolmer, W. Ko, A. De La Fuente Duran, S. Subramanian, C. Dong, J. Shallenberger, M. Fu, Q. Zou, Y. Chuang, Z. Gai, A. Li, A. Bostwick, C. Jozwiak, C. Chang, E. Rotenberg, J. Zhu, A. C. T. van Duin, V. Crespi, and J. A. Robinson, Nat. Mater. **19**, 637 (2020).

[29] S. Wundrack, N. Schmidt, D. M. Pakdehi, K. Pierz, L. Michaliszyn, H. Spende, A. Schmidt, H. W. Schumacher, R. Stosch, and A. Bakin, arXiv:1905.12438 (2019).

[30] M. Kruskopf, D. Momeni Pakdehi, K. Pierz, S. Wundrack, R. Stosch, T. Dziomba, M. Götz, J. Baringhaus, J. Aprojanz, C. Tegenkamp, J. Lidzba, T. Seyller, F. Hohls, F. J. Ahlers, and H. W. Schumacher, 2D Mater. **3**, 041002 (2016).

[31] D. Momeni Pakdehi, K. Pierz, S. Wundrack, J. Aprojanz, T. T. N. Nguyen, T. Dziomba, F. Hohls, A. Bakin, R. Stosch, C. Tegenkamp, F. J. Ahlers, and H. W. Schumacher, ACS Appl. Nano Mater. **2**, 844 (2019).

[32] D. Momeni Pakdehi, J. Aprojanz, A. Sinterhauf, K. Pierz, M. Kruskopf, P. Willke, J. Baringhaus, J. P. Stöckmann, G. A. Traeger, F. Hohls, C. Tegenkamp, M. Wenderoth, F. J. Ahlers, and H. W. Schumacher, ACS Appl. Mater. Interfaces **10**, 6039 (2018).

[33] See Supplemental Material at http://link.aps.org/supplemental/10.1103/PhysRevMaterials.5.024006 for further details about the topography of epitaxial graphene measured with AFM, the SEM picture of epitaxial graphene showing micropipes in SiC, phonon dispersion of Ga-intercalated QFBLG, the Raman spectrum of a Ga droplet, Raman mappings of Ga-intercalated graphene and the absence of lattice defects, the optical properties of a SiC/Ga/QFBLG heterostack using microreflectance and transmission microscopy, and a video of Ga-intercalation of epitaxial graphene (self-propagation of Ga) using optical microscopy at ambient conditions.

[34] M. S. Seifner, M. Sistani, F. Porrati, G. Di Prima, P. Pertl, M. Huth, A. Lugstein, and S. Barth, ACS Nano **12**, 1236 (2018).

[35] J. S. Becker and H. J. Dietze, Int. J. Mass Spectrom. **228**, 127 (2003).

[36] J. Colwell, P. Hsiao, W. Zhang, X. Wang, R. Akter, and A. Lennon, J. Anal. At. Spectrom. **33**, 422 (2018).

[37] P. H. Chi, F. H. Ko, C. T. Hsu, H. L. Chen, C. K. Yang, Y. C. Sun, and M. H. Yang, J. Anal. At. Spectrom. **17**, 358 (2002).

[38] M. H. Oliveira, T. Schumann, F. Fromm, R. Koch, M. Ostler, M. Ramsteiner, T. Seyller, J. M. J. Lopes, and H. Riechert, Carbon **52**, 83 (2013).

[39] C. Riedl, C. Coletti, T. Iwasaki, A. A. Zakharov, and U. Starke, Phys. Rev. Lett. **103**, 246804 (2009).

[40] J. D. Emery, V. H. Wheeler, J. E. Johns, M. E. McBriarty, B. Detlefs, M. C. Hersam, D. K. Gaskill, and M. J. Bedzyk, Appl. Phys. Lett. **105**, 161602 (2014).

[41] S. Wundrack, D. Momeni Pakdehi, P. Schädlich, F. Speck, K. Pierz, T. Seyller, H. W. Schumacher, A. Bakin, and R. Stosch, Phys. Rev. B **99**, 045443 (2019).

[42] J. F. Moulder and J. Chastain, *Handbook of X-Ray Photoelectron Spectroscopy: A Reference Book of Standard Spectra for Identification and Interpretation of XPS Data* (Physical Electronics Division, Perkin-Elmer Corporation, 1992).

[43] L. Cademartiri, M. M. Thuo, C. A. Nijhuis, W. F. Reus, S. Tricard, J. R. Barber, R. N. S. Sodhi, P. Brodersen, C. Kim, R. C. Chiechi, and G. M. Whitesides, J. Phys. Chem. C **116**, 10848 (2012).

[44] C. L. Hinkle, M. Milojevic, B. Brennan, A. M. Sonnet, F. S. Aguirre-Tostado, G. J. Hughes, E. M. Vogel, and R. M. Wallace, Appl. Phys. Lett. **94**, 162101 (2009).

[45] J. Ivanco, T. Kubota, and H. Kobayashi, J. Appl. Phys. **97**, 073712 (2005).

[46] M. Ostler, R. J. Koch, F. Speck, F. Fromm, H. Vita, M. Hundhausen, K. Horn, and T. Seyller, Mater. Sci. Forum **717-720**, 649 (2012).

[47] M. Ostler, F. Fromm, R. J. Koch, P. Wehrfritz, F. Speck, H. Vita, S. Böttcher, K. Horn, and T. Seyller, Carbon **70**, 258 (2014).

[48] M. Shur, S. Rumyantsev, and M. Levinshtein, *SiC Materials and Devices* (World Scientific, Singapore, 2006).

[49] J. Hassan, C. Virojanadara, A. Meyer, I. G. Ivanov, J. I. Flege, S. Watcharinyanon, J. Falta, L. I. Johansson, and E. Janzén, Mater. Sci. Forum **717-720**, 605 (2012).

[50] D. Momeni Pakdehi, P. Schädlich, T. T. N. Nguyen, A. A. Zakharov, S. Wundrack, F. Speck, K. Pierz, T. Seyller, C. Tegenkamp, and H. W. Schumacher, Adv. Funct. Mater. **30**, 2004695 (2020).

[51] A. C. Ferrari and D. M. Basko, Nat. Nanotechnol. **8**, 235 (2013).

[52] L. G. Cançado, A. Jorio, E. H. M. Ferreira, F. Stavale, C. A. Achete, R. B. Capaz, M. V. O. Moutinho, A. Lombardo, T. S. Kulmala, and A. C. Ferrari, Nano Lett. **11**, 3190 (2011).

[53] A. Eckmann, A. Felten, A. Mishchenko, L. Britnell, R. Krupke, K. S. Novoselov, and C. Casiraghi, Nano Lett. **12**, 3925 (2012).

[54] A. C. Ferrari and J. Robertson, Phys. Rev. B **64**, 075414 (2001).

[55] A. C. Ferrari and J. Robertson, Phys. Rev. B **61**, 14095 (2000).

[56] F. Fromm, M. H. Oliveira, A. Molina-Sánchez, M. Hundhausen, J. M. J. Lopes, H. Riechert, L. Wirtz, and T. Seyller, New J. Phys. **15**, 043031 (2013).

[57] C. H. Lui, L. M. Malard, S. Kim, G. Lantz, F. E. Laverge, R. Saito, and T. F. Heinz, Nano Lett. **12**, 5539 (2012).

[58] D. S. Lee, C. Riedl, B. Krauss, K. Von Klitzing, U. Starke, and J. H. Smet, Nano Lett. **8**, 4320 (2008).

[59] K. G. Steenbergen and N. Gaston, Chem. Commun. **55**, 8872 (2019).

[60] T. S. Grigera, V. Martín-Mayor, G. Parisi, and P. Verrocchio, Nature (London) **422**, 289 (2003).

[61] M. Ivanda, I. Hartmann, and W. Kiefer, Phys. Rev. B **51**, 1567 (1995).

[62] S. Y. Lee and H. C. Kang, J. Cryst. Growth **412**, 25 (2015).

[63] R. Li, G. Sun, and L. Xu, J. Chem. Phys. **145**, 054506 (2016).

[64] S. Pisana, M. Lazzeri, C. Casiraghi, K. S. Novoselov, A. K. Geim, A. C. Ferrari, and F. Mauri, Nat. Mater. **6**, 198 (2007).

[65] D. Das, S. Bhattacharyya, E. Muñoz, and A. K. Singh, Phys. Rev. B **94**, 115438 (2016).

[66] A. Das, S. Pisana, B. Chakraborty, S. Piscanec, S. K. Saha, U. V. Waghmare, K. S. Novoselov, H. R. Krishnamurthy, A. K. Geim, A. C. Ferrari, and A. K. Sood, Nat. Nanotechnol. **3**, 210 (2008).

[67] F. Ding, H. Ji, Y. Chen, A. Herklotz, K. Dörr, Y. Mei, A. Rastelli, and O. G. Schmidt, Nano Lett. **10**, 3453 (2010).

[68] J. E. Lee, G. Ahn, J. Shim, Y. S. Lee, and S. Ryu, Nat. Commun. **3**, 1024 (2012).

[69] C. Neumann, S. Reichardt, P. Venezuela, M. Drögeler, L. Banszerus, M. Schmitz, K. Watanabe, T. Taniguchi, F. Mauri, B. Beschoten, S. V. Rotkin, and C. Stampfer, Nat. Commun. **6**, 8429 (2015).

[70] L. J. van der PAUW, in *Semiconductor Devices: Pioneering Papers* (World Scientific, Singapore, 1991), pp.174–182.

[71] J. Ristein, S. Mammadov, and T. Seyller, Phys. Rev. Lett. **108**, 246104 (2012).

[72] A. Das, B. Chakraborty, S. Piscanec, S. Pisana, A. K. Sood, and A. C. Ferrari, Phys. Rev. B **79**, 155417 (2009).

[73] M. Petrović, I. Šrut Rakić, S. Runte, C. Busse, J. T. Sadowski, P. Lazić, I. Pletikosić, Z. H. Pan, M. Milun, P. Pervan, N. Atodiresei, R. Brako, D. Šokčević, T. Valla, T. Michely, and M. Kralj, Nat. Commun. **4**, 2772 (2013).